Universiteit Utrecht

Opleiding Natuur- en Sterrenkunde

Simulations of Magnetic Fields in Heavy Ion Collisions

Bachelor Thesis

Ruud Nimour

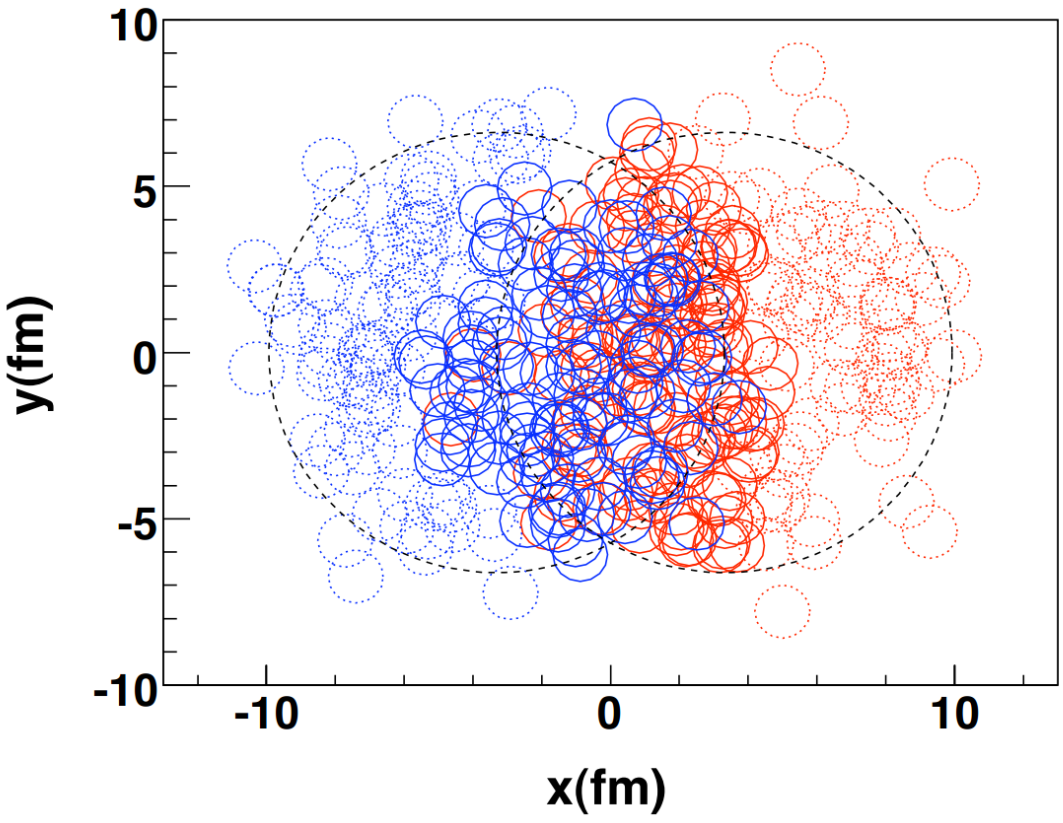

Supervisors:
Prof. R. Snellings
Institute of Subatomic Physics
MSc. Jacopo Margutti
Institute of Subatomic Physics

June, 2017

Abstract

The magnetic fields in relativistic heavy ion collisions can get up to 10^{15} T[1]. These fields become so huge because charges (protons) are moving at very high speeds very close to the observation point. In this thesis a program used to simulate relativistic heavy ion collisions, T$_{\mathrm{R}}$ENTo (*Reduced Thickness Event-by-Event Nuclear Topology* [2]), is used to simulate the magnetic field in heavy ion collisions, in order to study the spatial and time dependence of the magnetic field in such collisions. T$_{\mathrm{R}}$ENTo is a nice tool to simulate events because it already simulates different events by randomly placing nucleons in accordance to the *Woods-Saxon distribution*, an approximate nucleon density distribution for heavy atoms. The simulations carried out in this thesis give rise to a magnetic field of up to 10^{16} T. There are several differences between the results from T$_{\mathrm{R}}$ENTo and the existing literature, but T$_{\mathrm{R}}$ENTo seems to be working as intended, and gives results which are expected.

Source for the figure of the title page: [3], figure 1. Typical event for Pb+Pb collisions.

Contents

1 Introduction

In the Large Hadron Collider (LHC), heavy ions are collided at relativistic speeds in order to try to create a quark-gluon plasma (QGP), which is a highly exotic state of matter which was the state of the universe for only a few millionths of a second after the Big Bang [4]. Whereas everyday matter is made of protons and neutrons and electrons, inside the QGP the temperatures and densities are so high that not only the electrons break free from their nuclei, but also the quarks which make up atoms—and are very tightly bound together by gluons—break loose and form a state of matter which is called a QGP. The only places on earth where such extremely high temperatures and pressures are currently experimentally recreated, are in the Relativistic Heavy Ion Collider (RHIC) at the Brookhaven National Laboratory (BNL) and in the LHC [5].

An interesting quantum effect that may occur in a QGP is the *Chiral Magnetic Effect* (CME)[6]. In extreme magnetic fields, such as those arising in heavy ion collisions, in certain field configurations characterized by a so-called winding number[1], the CME effectively separates charge along the magnetic field, that is, an electric current is produced as a result of quantum effects.

The aim of this thesis is to model the magnetic field at the moment of collision of heavy ions, and for a short while (about 1 fm/c) after the impact. While this has been done before [1, 5, 8, 9], in this thesis we modified T$_{\text{R}}$ENTo , a program originally intended for the creation and inspection of density profiles of heavy ion collisions [2], to investigate the space and time dependence of the magnetic field. While qualitatively the same results as in the existing literature about this subject has been found, we find some differences between the results from T$_{\text{R}}$ENTo and the existing literature. However these differences are explained and make sense.
We will try to study the nature of the magnetic field in those heavy ion collisions. In our case we analyze lead-lead collisions at beam energy per nucleon pair $\sqrt{s_{NN}} = 2.76$ TeV. These are the energies at which the LHC operates to create a quark-gluon plasma [10]. The magnetic field is analyzed as a function of impact parameter, time, and position in this thesis, and compared to other simulations.

In the next sections the CME is explored a bit more, the relativistically correct expression for the magnetic field is derived from the Liénard-Wiechert potentials, and a detailed overview of T$_{\text{R}}$ENTo is provided, after which the magnetic fields obtained with T$_{\text{R}}$ENTo as a function of impact parameter, time, and position are compared with existing literature and discussed.

2 Theory

2.1 Chiral Magnetic Effect

The dynamics of a quark-gluon plasma is described by quantum chromodynamics (QCD). An interesting prediction of QCD is that certain gluon configurations give rise to a winding number, which is a topological invariant. This means that smooth deformations of such gluon configurations will not change this winding number. At high temperatures, such configurations with nonzero winding number can be produced with relatively high probability [11].

In [6], section 4 it is shown that such configurations can separate charge in presence of a magnetic field. The situation in which the magnetic field is assumed to be very large from [6] is worth explaining here, to try and give an intuitive feeling as to how this can take place.
Since the magnetic field is assumed to be extreme, all particles can only move along the magnetic field, and will have their spin parallel with the magnetic field. Quarks with opposite charges have their spin antiparallel to the magnetic field. Here is where the chirality plays a role, it inverts this relationship: right-handed positively charged fermions and left-handed negatively charged fermions are parallel to the magnetic field, whereas right-handed negatively charged particles and left-handed postively charged particles are antiparallel to the magnetic field. If some of the fermions

[1] For details see reference [6], the important part here is that the winding number is an integer which cannot be smoothly transformed into another, some say it is *topologically protected* [7].

will then change their chirality due to the effects of a nonzero winding number configuration, the fermions which change chirality can only do so by flipping their momentum, since flipping their spin is energetically impossible due to the extreme magnetic field. This idealized situation is seen in figure 1.

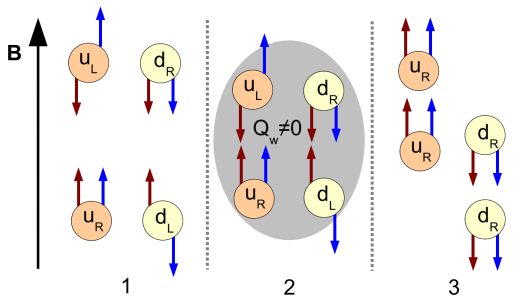

Figure 1: Illustation of the Chiral Magnetic Effect in a very large magnetic field. The red arrows denote the direction of momentum, the blue arrows denote the spin of the quarks. *Source:* [6], figure 1.

At this point we see that flipping momentum of only left-handed fermions into right-handed fermions causes an electric charge imbalance: positive charges moving downwards now go upward, and negative charges going upward now go downward. We see a net current moving along the magnetic field. This is the Chiral Magnetic Effect.

The winding number only changes left-handed particles into right-handed ones because the sign of the winding number determines whether the configurations can change left-handed into right-handed or vice versa [6, 11]. The explanation for this comes from quantum field theory, but that goes beyond the scope of this thesis. Another detail, is that this change in charge distribution causes an electric field, which could move the charges back. however this effect will only be a small suppression of the CME, because the resulting electric field will be very small, since the number of particles to which this happens is actually very small [6].

2.2 The Magnetic Field

In order to model the magnetic fields in relativistic heavy ion collisions, one must use relativistic electrodynamics. In the simplistic model used in TRENTo for the magnetic field of a heavy ion collision, protons will be treated as point particles, and neutrons will be effectively ignored. This should serve as a decent approximation, and considering the constituent quarks and quantum effects is out of scope of this project. Since this is such an integral part to this thesis, it may be nice to derive the expression for the electric and magnetic field of a relativistic point particle. We will start from the well-known Liénard-Wiechert potentials [12, 13]:

$$\boldsymbol{A}(\boldsymbol{r},t) = \frac{q}{4\pi\varepsilon_0 c}\left[\frac{\boldsymbol{\beta}}{R-\boldsymbol{R}\cdot\boldsymbol{\beta}}\right]_{t=t'}, \tag{1}$$

$$\text{where } t' = t - \frac{R(t')}{c}. \tag{2}$$

Here $\boldsymbol{A}$ is the vector potential (so that $\nabla\times\boldsymbol{A}=\boldsymbol{B}$). ε_0 is the magnetic permittivity of the vacuum, c the speed of light, q the charge of the moving particle. $R=|\boldsymbol{R}|$, where $\boldsymbol{R}$ is the vector from the charge to the observation point (i.e. $\boldsymbol{R}=\boldsymbol{r}-\boldsymbol{r}_c$)[2]. and lastly $\boldsymbol{\beta}=\boldsymbol{v}/c=\dot{\boldsymbol{r}}_c/c$ the velocity as usual. Note that the quantities in square brackets should be evaluated at the retarded time t', defined implicitly by equation 2.

[2] c here stands for charge

2.2.1 The Calculation

To extract the magnetic field $\boldsymbol{B}$, we take the curl of the vector potential $\boldsymbol{A}$:

$$\begin{aligned}\boldsymbol{B} = \nabla \times \boldsymbol{A} &= \frac{q}{4\pi\varepsilon_0 c} \cdot \nabla \times \left[\frac{\boldsymbol{\beta}}{R - \boldsymbol{R}\cdot\boldsymbol{\beta}}\right] \\ &= \frac{q}{4\pi\varepsilon_0 c} \cdot \left[\frac{\nabla\times\boldsymbol{\beta}}{R-\boldsymbol{R}\cdot\boldsymbol{\beta}} - \frac{\Big(\nabla(R-\boldsymbol{R}\cdot\boldsymbol{\beta})\Big)\times\boldsymbol{\beta}}{(R-\boldsymbol{R}\cdot\boldsymbol{\beta})^2}\right] \\ &= \frac{q}{4\pi\varepsilon_0 c} \cdot \left[\frac{\nabla\times\boldsymbol{\beta}}{R-\boldsymbol{R}\cdot\boldsymbol{\beta}} - \frac{\Big(\nabla R - \nabla(\boldsymbol{R}\cdot\boldsymbol{\beta})\Big)\times\boldsymbol{\beta}}{(R-\boldsymbol{R}\cdot\boldsymbol{\beta})^2}\right] \end{aligned} \tag{3}$$

Several vector calculus identities were used. Now each term in the brackets must be evaluated. First the curl of $\boldsymbol{\beta}$. Consider the x-component of $\nabla\times\boldsymbol{\beta}$:

$$(\nabla\times\boldsymbol{\beta})_x = \partial_y\beta_z - \partial_z\beta_y = \dot\beta_z\partial_y t' - \dot\beta_y\partial_z t' = (\dot{\boldsymbol{\beta}}\times(\nabla t'))_x.$$

Other components go the same way, and we obtain

$$\nabla\times\boldsymbol{\beta} = \dot{\boldsymbol{\beta}}\times(\nabla t') \tag{4}$$

For ∇R, note that $c(t-t') = R$ (see equation 2), so we find:

$$\nabla R = \nabla c(t-t') = -c\nabla t'. \tag{5}$$

For $\nabla(\boldsymbol{R}\cdot\boldsymbol{\beta})$, we consider again the x-component:

$$\begin{aligned}\Big(\nabla(\boldsymbol{R}\cdot\boldsymbol{\beta})\Big)_x &= \partial_x\Big((x-x_c)\beta_x + (y-y_c)\beta_y + (z-z_c)\beta_z\Big) \\ &= \beta_x + \Big((x-x_c)\dot\beta_x - \dot x_c\beta_x + (y-y_c)\dot\beta_y - \dot y_c\beta_y + (z-z_c)\dot\beta_z - \dot z_c\beta_z\Big)\partial_x t' \\ &= \beta_x + \Big(\boldsymbol{R}\cdot\dot{\boldsymbol{\beta}} - \boldsymbol{\beta}c\cdot\boldsymbol{\beta}\Big)\partial_x t' = \Big(\boldsymbol{\beta} + \Big(\boldsymbol{R}\cdot\dot{\boldsymbol{\beta}} - \boldsymbol{\beta}^2 c\Big)\nabla t'\Big)_x.\end{aligned}$$

Other components go likewise, and we obtain:

$$\nabla(\boldsymbol{R}\cdot\boldsymbol{\beta}) = \boldsymbol{\beta} + \Big(\boldsymbol{R}\cdot\dot{\boldsymbol{\beta}} - \boldsymbol{\beta}^2 c\Big)\nabla t' \tag{6}$$

Seeing how all previous expressions depend on $\nabla t'$, we will calculate that now, by applying ∂_x to equation 2:

$$\begin{aligned}\partial_x t' = -\frac{1}{c}\partial_x R &= -\frac{1}{c}\partial_x[(x-x_c)^2 + \ldots]^{1/2} \\ &= -\frac{1}{c}\left(\frac{(x-x_c)\partial_x(x-x_c) + (y-y_c)\partial_x(y-y_c) + (z-z_c)\partial_x(z-z_c)}{[(x-x_c)^2+\ldots]^{1/2}}\right) \\ &= -\frac{1}{c}\left(\frac{x-x_c}{[(x-x_c)^2+\ldots]^{1/2}} - \frac{[(x-x_c)\cdot\dot x_c + \ldots + \ldots]\,\partial_x t'}{[(x-x_c)^2+\ldots]^{1/2}}\right) \\ &= -\frac{1}{c}\left(\frac{\boldsymbol{R}}{R}\right)_x + \frac{1}{c}\left(\frac{\boldsymbol{R}\cdot\boldsymbol{\beta}c}{R}\right)\partial_x.\end{aligned}$$

So we obtain, multiplying by R on both sides:

$$\partial_x t'(R - \boldsymbol{R}\cdot\boldsymbol{\beta}) = -\frac{1}{c}\boldsymbol{R}_x \quad\Rightarrow\quad \partial_x t' = -\frac{\boldsymbol{R}_x/c}{R-\boldsymbol{R}\cdot\boldsymbol{\beta}}.$$

Again, other components go likewise so we end up with

$$\nabla t' = -\frac{\boldsymbol{R}/c}{R - \boldsymbol{R}\cdot\boldsymbol{\beta}}. \tag{7}$$

Now it's time to put equations 4, 5, and 6 together in equation 3, where we ignore the prefactor $q/4\pi\varepsilon_0 c$ for now. We calculate:

$$\begin{aligned}
&\frac{\nabla\times\boldsymbol{\beta}}{R-\boldsymbol{R}\cdot\boldsymbol{\beta}} - \frac{\Big(\nabla R - \nabla(\boldsymbol{R}\cdot\boldsymbol{\beta})\Big)\times\boldsymbol{\beta}}{(R-\boldsymbol{R}\cdot\boldsymbol{\beta})^2} \\
&= \frac{\dot{\boldsymbol{\beta}}\times(\nabla t')}{R-\boldsymbol{R}\cdot\boldsymbol{\beta}} - \frac{\Big(-c\nabla t' - \cancelto{0}{\boldsymbol{\beta}} - \Big(\boldsymbol{R}\cdot\dot{\boldsymbol{\beta}} - \boldsymbol{\beta}^2 c\Big)\nabla t'\Big)\times\boldsymbol{\beta}}{(R-\boldsymbol{R}\cdot\boldsymbol{\beta})^2} \\
&= \frac{\dot{\boldsymbol{\beta}}\times(\nabla t')}{R-\boldsymbol{R}\cdot\boldsymbol{\beta}} + \frac{\Big(\boldsymbol{R}\cdot\dot{\boldsymbol{\beta}} + (1-\boldsymbol{\beta}^2)c\Big)(\nabla t')\times\boldsymbol{\beta}}{(R-\boldsymbol{R}\cdot\boldsymbol{\beta})^2}.
\end{aligned}$$

The $\boldsymbol{\beta}$ is crossed out because $\boldsymbol{A}\times\boldsymbol{A} = \boldsymbol{0}$ for any vector $\boldsymbol{A}$. Now we are almost there, we fill in $\nabla t'$ from equation 7 and rearrange:

$$\begin{aligned}
&= \frac{\dot{\boldsymbol{\beta}}\times(-\frac{\boldsymbol{R}/c}{R-\boldsymbol{R}\cdot\boldsymbol{\beta}})}{R-\boldsymbol{R}\cdot\boldsymbol{\beta}} + \frac{\Big(\boldsymbol{R}\cdot\dot{\boldsymbol{\beta}} + (1-\boldsymbol{\beta}^2)c\Big)(-\frac{\boldsymbol{R}/c}{R-\boldsymbol{R}\cdot\boldsymbol{\beta}})\times\boldsymbol{\beta}}{(R-\boldsymbol{R}\cdot\boldsymbol{\beta})^2} \\
&= \frac{\boldsymbol{R}\times\dot{\boldsymbol{\beta}}/c}{(R-\boldsymbol{R}\cdot\boldsymbol{\beta})^2} + \frac{\Big(\boldsymbol{R}\cdot\dot{\boldsymbol{\beta}}/c + (1-\boldsymbol{\beta}^2)\Big)(\boldsymbol{\beta}\times\boldsymbol{R})}{(R-\boldsymbol{R}\cdot\boldsymbol{\beta})^3} \\
&= \frac{(R-\boldsymbol{R}\cdot\boldsymbol{\beta})(\boldsymbol{R}\times\dot{\boldsymbol{\beta}}/c) + \Big(\boldsymbol{R}\cdot\dot{\boldsymbol{\beta}}/c + (1-\boldsymbol{\beta}^2)\Big)(\boldsymbol{\beta}\times\boldsymbol{R})}{(R-\boldsymbol{R}\cdot\boldsymbol{\beta})^3} \\
&= \frac{(1-\boldsymbol{\beta}^2)(\boldsymbol{\beta}\times\boldsymbol{R})}{(R-\boldsymbol{R}\cdot\boldsymbol{\beta})^3} + \frac{\boldsymbol{R}\times\Big[(R-\boldsymbol{R}\cdot\boldsymbol{\beta})(\dot{\boldsymbol{\beta}}/c) + \Big(\boldsymbol{R}\cdot\dot{\boldsymbol{\beta}}/c\Big)(\boldsymbol{\beta})\Big]}{(R-\boldsymbol{R}\cdot\boldsymbol{\beta})^3}.
\end{aligned}$$

Now we introduce the Lorentz factor $\gamma = (1-\beta^2)^{-1/2}$. Next we will simplify second term by using the BAC - CAB rule in reverse, i.e. $\boldsymbol{B}(\boldsymbol{A}\cdot\boldsymbol{C}) - \boldsymbol{C}(\boldsymbol{A}\cdot\boldsymbol{B}) = \boldsymbol{A}\times(\boldsymbol{B}\times\boldsymbol{C})$ for vectors $\boldsymbol{A},\boldsymbol{B},\boldsymbol{C}$.

$$\begin{aligned}
&= \frac{(\boldsymbol{\beta}\times\boldsymbol{R})}{\gamma^2(R-\boldsymbol{R}\cdot\boldsymbol{\beta})^3} + \frac{\boldsymbol{R}\times\Big[\frac{R}{c}\dot{\boldsymbol{\beta}} - (\boldsymbol{R}\cdot\boldsymbol{\beta})(\dot{\boldsymbol{\beta}}/c) + \Big(\boldsymbol{R}\cdot\dot{\boldsymbol{\beta}}/c\Big)(\boldsymbol{\beta})\Big]}{(R-\boldsymbol{R}\cdot\boldsymbol{\beta})^3} \\
&= \frac{(\boldsymbol{\beta}\times\boldsymbol{R})}{\gamma^2(R-\boldsymbol{R}\cdot\boldsymbol{\beta})^3} + \frac{\boldsymbol{R}\times\Big[R\dot{\boldsymbol{\beta}} + \boldsymbol{R}\times(\dot{\boldsymbol{\beta}}\times\boldsymbol{\beta})\Big]}{c(R-\boldsymbol{R}\cdot\boldsymbol{\beta})^3}
\end{aligned}$$

Thus, we arrive at the final expression for the magnetic field:

$$\boldsymbol{B} = \frac{q}{4\pi\varepsilon_0 c}\left[\frac{(\boldsymbol{\beta}\times\boldsymbol{R})}{\gamma^2(R-\boldsymbol{R}\cdot\boldsymbol{\beta})^3} + \frac{\boldsymbol{R}\times\Big[R\dot{\boldsymbol{\beta}} + \boldsymbol{R}\times(\dot{\boldsymbol{\beta}}\times\boldsymbol{\beta})\Big]}{c(R-\boldsymbol{R}\cdot\boldsymbol{\beta})^3}\right]_{t=t'}. \tag{8}$$

For completeness, most variables are already defined under equation 1, $\gamma = (1-\beta^2)^{-1/2}$ is the Lorentz factor, and the dot over $\boldsymbol{\beta}$ represents the derivative with respect to its argument t'. Note how only the left term in brackets survives if a charged particle doesn't accelerate ($\dot{\boldsymbol{\beta}} = 0$).

3 T$_R$ENTo

In order to simulate the heavy ion collisions, we modified T$_R$ENTo. T$_R$ENTo stands for *Reduced Thickness Event-by-Event Nuclear Topology* [2]. It is an open-source program written in C++, capable of simulating thousands of events in seconds on an ordinary desktop computer. The events it simulates are snapshots of collisions of protons, deuterons, lead, gold or uranium. It features an option to customize any heavy ion one could want as well. We modified it such that instead of these event snapshots, it writes the impact parameter and the magnetic field at multiple places of an event in plain text.

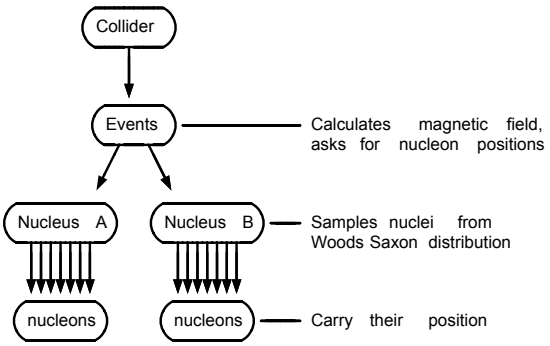

Figure 2: A very simplified diagram of the main structure of T$_R$ENTo classes.

Originally, the model was constructed to simulate the so-called thickness of proton-proton, ion-proton, or ion-ion collisions [2]. This thickness is essentially the density of matter at the moment of collision, not taking into account whether the particles are neutrons or protons. Up to fifth order the eccentricities of this thickness profile are calculated, which can be used to model the elliptic flow of the QGP [14].

The source files of T$_R$ENTo are sorted in *header* (*.h*)-files and *.cxx*-files. This is standard C++ practice, as writing classes in multiple files keeps the program organized, and faster to compile. In order for one class to access another class' methods (i.e. functions) or members, it needs to know what methods and members other classes have. This is achieved by including the headers of other classes needed, which declare methods and members but do not initialize them (i.e. headers tell what things a class has, but do not tell what they do).
The source files of T$_R$ENTo are written to be easily installed on Ubuntu and other Linux distributions, using *CMake*.

A detailed analysis of T$_R$ENTo can be found in the rest of this chapter[3]. A very simple diagram of the structure of T$_R$ENTo can be seen in figure 2.

3.1 Classes

The most important classes (with a brief description) of T$_R$ENTo are as follows:

Trento *Trento* is the main body of the program, where user input (type of colliding particles, number of events etc.) is converted into the desired actions.

Output In the *Output* class, the program sorts the output of the events in a file. There is also an option to create a folder which contains each event and corresponding nuclear thickness in a separate file, but this feature is not used.

Collider The *Collider* class produces events with two nuclei. It samples random impact parameters until a collision occurs, and then forwards that data to the *Event* class.

Event In the *Event* class, all the main calculations occur. It takes two *Nuclei* and their randomly positioned nucleons and calculates the magnetic contribution from each nucleon.

Nucleus An *Event* happens between two Nuclei. The *Nucleus* class carries the information a Nucleus needs to have: what kind of nucleus, so the number of nucleons it has, and its shape.

Nucleon The *Nucleon* is what makes up the Nucleus, and several variables are stored here, such as most notably charge and position.

[3]The online documentation of the unmodified T$_R$ENTo can be found in reference [15].

3.1.1 Event

A large portion of the original *Event* class has been removed, because it used to calculate the particle density on a grid, which is not the focus of this thesis. In the current state of the program, the *Event* class has been modified such that it contains just the methods needed to calculate the magnetic field, as described by equation 8.

The main method that is used by the *Collider* (compute), requests two *Nuclei*, and runs through each nucleon per nucleus and calculates the individual magnetic contribution of that nucleon if the particle is charged, and if the particle is not too close to the observation point[4]. This is done to prevent a single proton very close to the observation point dominating the magnetic field, because $B \sim 1/R^2$ (which goes to infinity as $R \to 0$), and measuring the magnetic field of a proton inside itself makes no sense anyway, since we model the protons as point charges, rather than made of quarks.

In order to create graphs for the magnetic field at different positions, the code is adjusted so that every event runs through the magnetic field calculation cycle a couple of times, but at different points. For example, in figure 11, the x- and y-direction of the magnetic field is calculated at (-12,0) fm, (-11,0) fm, ..., (12,0) fm. These magnetic fields are then stored in an array specific to that event, so that the *Output* class can write the magnetic field in the x- and y-direction per event.

3.1.2 Nucleus

T$_{\text{R}}$ENTo simulates the fluctuations of nucleons within a nucleus. T$_{\text{R}}$ENTo essentially chooses random points inside a sphere with a probability in accordance to the Woods-Saxon distribution [17]. The event is just a 2-dimensional snapshot, i.e. the nucleon positions are projected onto the reaction plane, or equivalently, only the x- and y-coordinates are stored. This is done because at ultra-relativistic speeds, the nuclei Lorentz contract in the direction of their motion, which makes them very flat[5], so the size along their motion is negligible.

T$_{\text{R}}$ENTo does also, however, have the ability to model nuclei which are significantly differ from a spherical distribution, such as the deformed Woods-Saxon distribution. Uranium nuclei may actually be more accurately described by this[2]. There is also a preset deformed copper nucleus. If these deformed nuclei are used, it could bring more fluctuation in the magnetic fields, since now each nucleus in a collision will have an orientation, which changes the way the nucleons are distributed, which changes the magnetic field. However since this thesis restricts to considering lead-lead collisions at $\sqrt{s_{NN}} = 2.76$ TeV, we do not use this feature.

3.1.3 Nucleon

The *Nucleon* class only needs to store its position and charge, and whether it is a participant or not. It also contains some functions which care about the thickness profile, which are not used. Because the *nucleon* functions are called very often, and are short (e.g. `double Nucleon::x() const { return x_; }`), they are inlined. This means that, when this function `x()` is called, rather than going to the definition of `x()` to execute it, the definition of `x()` is *replaced* everywhere where the `x()` is called. This reduces the function call time, as the function is no longer called in the traditional sense, but rather replaced at *compile time*.

[4] *Too close* here is 0.3 fm, which is also used in [16]. Varying this exclusion radius did change the result significantly, unlike in [16]. See the section 4.1.1 for details.

[5] for lead-lead collisions at $\sqrt{s_{NN}} = 2.76$ TeV, the Lorentz factor is about 1470, so given a nuclear radius of ≈ 6.62 fm, we see the nucleus is only 2×6.62 fm $/1470 \approx 0.009$ fm thick.

3.1.4 Collider

The *Collider* class runs as many events as requested on the command line. In this class the impact parameter b is sampled from a probability density function $P(b) \sim b$, so there are very few impact parameters sampled for low b, but when b becomes too large, there is a chance that no collision will occur, and another random b is chosen from the same probability density function. This leads to most impact parameters being around 13 fm, after which the chances of collision occurring are drastically reduced. This is because the radius of lead nuclei has been set to 6.62 fm. See figure 3.

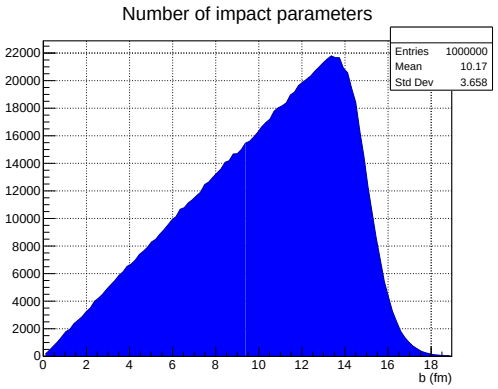

Figure 3: The number of events per impact parameter. The bins are 0.2 fm wide, and a total of 120000 events we sampled.

3.2 The Magnetic Field

The implementation of the magnetic field is done as follows: every nucleon stores whether it's a proton or not, so if yes, the calculation is continued. Then it is checked if the distance from the observation point to the proton is smaller the predefined exclusion radius, which we chose at $r_{\text{excl}} = 0.3$ fm, similar to in [16]. If yes, its magnetic contribution is not calculated (as stated in section 3.1.1), in order to prevent singularities. Then the speed vector $\boldsymbol{\beta}$ is determined (each nucleon has the same speed, up to a minus sign), and next, equation 8 gives the magnetic field. The term with the time derivative of the speed is ignored, since in this simple model, the participant nuclei are assumed keep moving at constant speed, and then come to a stop immediately upon impact[6]

[6] In the discussion (section 5), a slightly more sophisticated model is discussed, but shows little effect on the magnetic field, so we keep our analysis to the simplified model.

4 Results

4.1 Impact Parameter Dependence

For reference to what we would expect, see figure 4 (*source:* [5]). Here the magnetic field B as a function of impact parameter b is plotted. On the vertical axis eB/m_π^2 is plotted. 1 $m_\pi^2 \approx 10^{14}$ T in natural units[1][7]. The black line corresponds to the average net magnetic field per in the y-direction, whereas the colored lines correspond to the average absolute value of the magnetic field per event. We see that at zero impact parameter, though the average net magnetic field is zero, the average magnitude of the magnetic field is significant.

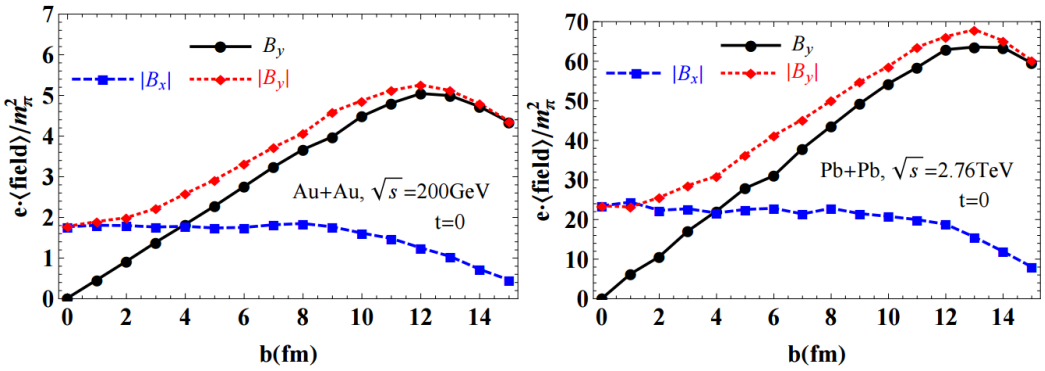

Figure 4: The magnetic field components in natural units at the center of the collision at $t = 0$, as functions of the impact parameter b. *Source:* [5], figure 1.

With T$_\text{R}$ENTo 120000 events with impact parameter between 0 and 15 fm[8] were simulated, and the corresponding average magnetic field per impact parameter is plotted in figure 5. For convenience, the same color scheme as in figure 4 is used. We see many of the same features as in figure 4. At zero impact parameter, the net magnetic field is zero on average while the average magnitude of the magnetic field in the x- and y-direction is about the same. As we look at events with a higher impact parameter, the average net magnetic field in the y-direction grows linearly, until it reaches a peak and decreases, at which point the average magnitude of the magnetic field in the x-direction drops off too.

All of this makes sense, at zero impact parameter we expect a zero net magnetic field on average, since there is no preferred direction. This does not mean that in a single event the magnetic field is zero on average, since by chance more protons can be on one side than the other. This gives rise to fluctuations per event, hence nonzero average magnitude of magnetic field.
The maximum of the magnetic field in the y-direction is around the point where almost all nucleons from one nucleus are on one side, and the nucleons from the other nucleus is on the other side. At this point, we can treat the nucleus as one big charge, giving rise to a $1/R^2$ drop-off which seems to be the case in the figure.

There are two striking differences between figure 4 and the T$_\text{R}$ENTo-generated 5. First is the order of magnitude. T$_\text{R}$ENTo gives a peak magnetic field of about 9×10^{16} T, whereas we expect about 65 m_π^2, equivalent to about 6.5×10^{15} T.
The second is the impact parameter at which we have maximum magnetic field. With T$_\text{R}$ENTo we find the peak is at about 9 fm, while from figure 4 we expect the peak at about 12 fm. These differences and possible causes will be discussed in section 5.

[7] A quick calculation verifies this: because $c = \hbar = e^2/4\pi\alpha = 1$, where $\alpha \approx 1/137$ is the fine structure constant, we find $m_\pi^2 = (140\text{ MeV}/c^2)^2 \overset{\text{natural units}}{=} (140\text{ MeV}/c^2)^2 \times c^2\sqrt{4\pi\alpha}/(e\hbar) \approx 1.0033 \times 10^{14}$ T.

[8] Even though the radius of a lead nucleus is only 6.62 fm, a collision between two lead nuclei further than 13.24 fm apart can still occur due to some nucleons sticking out far enough to hit the other nucleus.

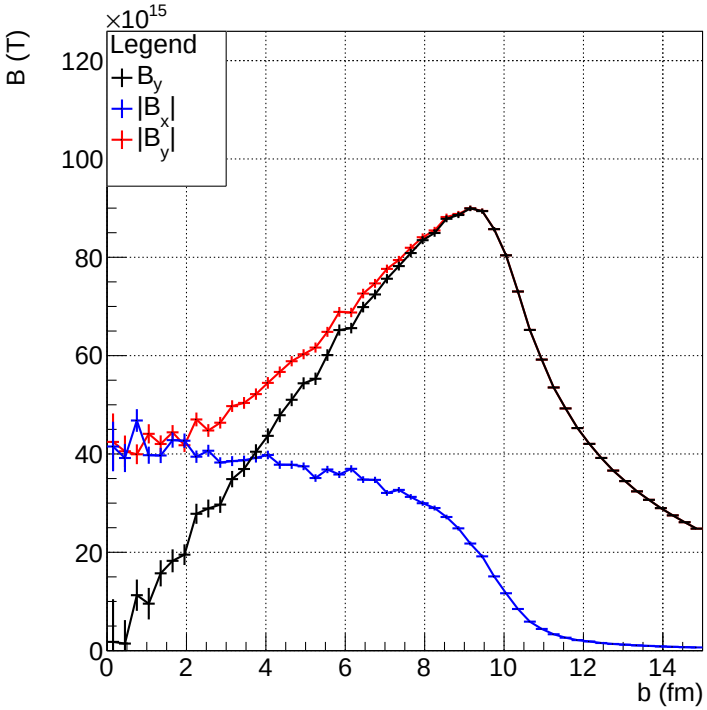

Figure 5: The (magnitude of) the magnetic field, averaged over 120000 events, in Pb+Pb collisions with $\sqrt{s_{NN}} = 2.76$ TeV at the center of the collision at $t = 0$, as function of the impact parameter b are shown here. The same color scheme is chosen as in figure 4.

4.1.1 Exclusion Radius Dependence

Because the magnetic field depends on the distance as $B \sim 1/R^2$, and because charges can get arbitrarily close to the observation point, in principle the magnetic field could be arbitrarily large. However, as noted in section 3.1.1, an exclusion radius of 0.3 fm was implemented, i.e. protons closer than 0.3 fm to the observation point are ignored. The results with no exlcusion radius and with a smaller exclusion radius of 0.1 fm can be seen in figure 6. With no exclusion radius, a single proton from a single event getting extremely close to the observation point can dominate the magnetic field of an entire bin in the histogram. This renders the histogram useless for analysis, as most of the magnetic field is just noise.
Note how in figure 6, plot (b), the average of $|B_x|$ and $|B_y|$ is much larger at smaller impact parameters. This makes sense, because in collisions with smaller impact parameters it is more likely that protons are within 0.1 and 0.3 fm of the center of the collision (the observation point). Exactly if this happens, their magnetic contribution is counted in 6, plot (b), but not in 5. This can cause changes in the appearance of the graph (which we see), because the biggest contribution of the magnetic field come from the protons which are closest to the observation point.

The results for larger exclusion radii (0.6 fm and 1 fm) can be seen in figure 7. Because more and more protons are ignored in the calculation of the magnetic field, the average magnetic field drops. This is especially seen at low impact parameters, when most of the protons are likely to be inside the exclusion radius, as explained above. The peak of the magnetic field with respect to the impact parameter also drops a bit (since we ignore more protons).
The rest of the tests will be done with an exclusion radius of 0.3 fm, as [16] uses this as well, and the results T$_\mathrm{R}$ENTo provides seems to match up best with figure 4.

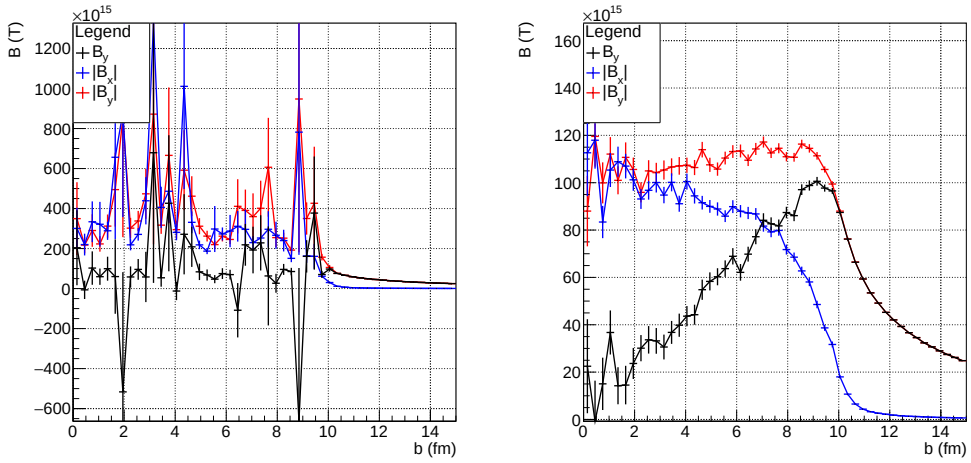

(a) **(b)**

Figure 6: The (magnitude of) the magnetic field, averaged over 120000 events, in Pb+Pb collisions with $\sqrt{s_{NN}} = 2.76$ TeV at the center of the collision at $t = 0$, as function of the impact parameter b are shown here.
(a) No exclusion radius is implemented. This gives rise to extreme fluctuations, as a single proton from a single event may dominate the average magnetic field of a single bin in the histogram (note how the error bars are relatively big).
(b) An exclusion radius of 0.1 fm is implemented. The extreme fluctuations are not present, though the magnitude of the magnetic field per event is much larger than in figure 5, especially at small impact parameters. The peak of B_y is still at 9 fm and has the same magnitude as before, though.

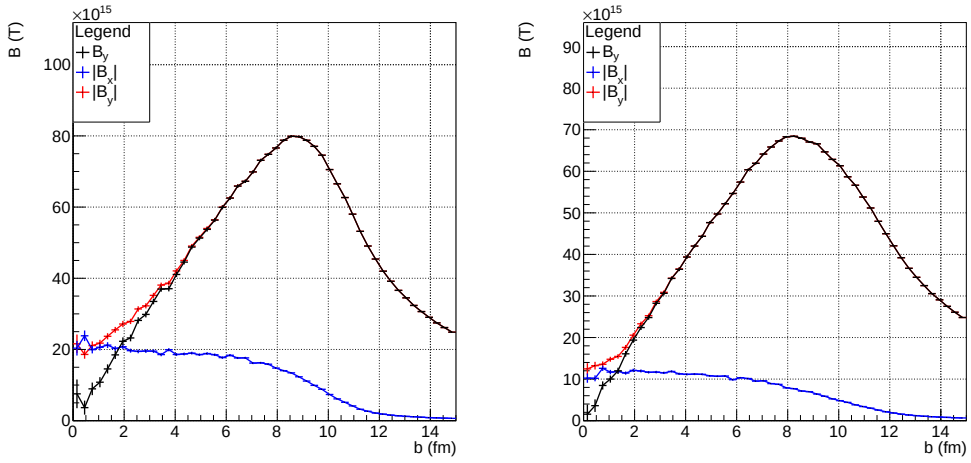

(a) **(b)**

Figure 7: The (magnitude of) the magnetic field, averaged over 120000 events, in Pb+Pb collisions with $\sqrt{s_{NN}} = 2.76$ TeV at the center of the collision at $t = 0$, as function of the impact parameter b are shown here.
(a) An exclusion radius of 0.6 fm is implemented. The average of $|B_x|$ and $|B_y|$ is smaller than in figure 5, also B_y lines up with $|B_y|$ sooner (i.e. there are fewer events with a negative B_y).
(b) An exclusion radius of 1 fm is implemented. same as above, but the effects are larger.

4.2 Time Dependence

For reference to what we would expect, see figure 8. Note that the vertical axis is logarithmic, and yet we see a very sharp peak around the collision time. Judging from the plot, we expect the magnetic field in lead-lead collisions to drop off with a factor of about 10^4 within 0.1 fm/c. Also, the remnants of the collision move slower than the original beam, and will bring an contribution to the magnetic field, visible after 0.1 fm/c in the right plot of 8. The remnants will give rise to an average magnetic field per event of about 0.01 m_π^2, corresponding to 10^{12} T.

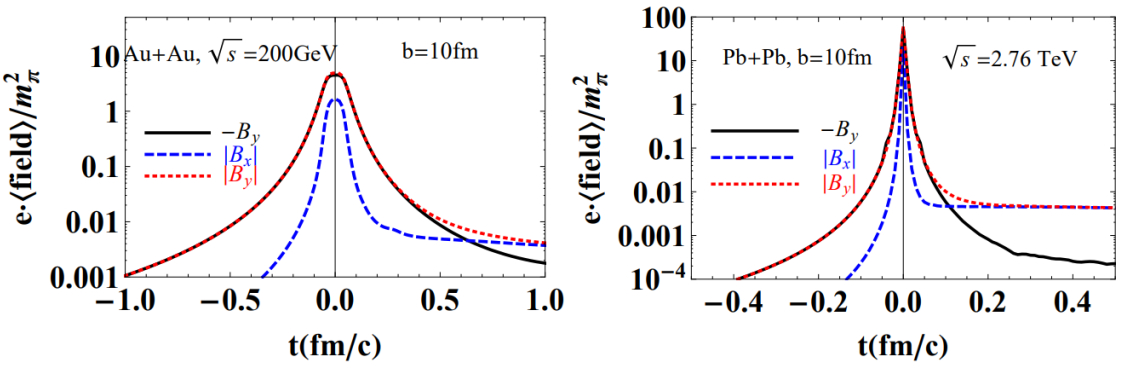

Figure 8: The magnetic field components in natural units at the center of the collision as functions of time. *Source:* [5], figure 2.

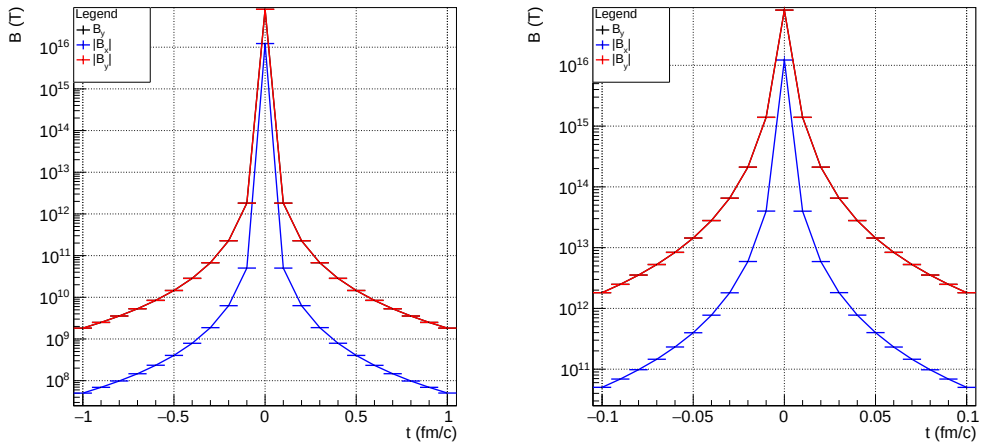

Figure 9: The time evolution of Pb+Pb collisions with $\sqrt{s_{NN}} = 2.76$ TeV is shown here. Note that the y-axis is logarithmic. The same color scheme is chosen as in figure 8. Plotted are the average magnetic field components over 120000 simulated events. On the left the time goes from -1 fm/c to +1 fm/c, and on the right for more detail the time goes from -0.1 fm/c to +0.1 fm/c.

The T$_\mathrm{R}$ENTo-generated time dependence also drops off with a factor of about 10^4 within 0.1 fm/c. However, there seems to be no contribution due to remnants. This is most likely because the implemented scattering of nucleons was that defined by equation A.7 in [6]. The scattering is very light however, as most nucleons keep moving roughly in the same direction, so the effect is barely noticeable in the plots.

4.3 x- and y-dependence

To get a feel for how we expect the magnetic fields to look like, see figure 10 (*source:* [8], figure 2). Essentially the moving nucleus is a moving charge, so it can be viewed as a current. This current induces a magnetic field around itself. In the center of the collision, the magnetic fields add up.

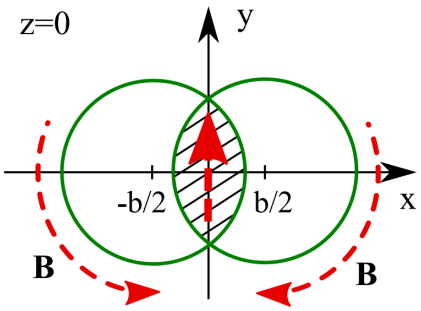

Figure 10: Simple diagram showing expected magnetic fields. *Source:* [8], figure 2.

The magnetic field was calculated with T$_{\mathrm{R}}$ENTo along the x- and y-axis for impact parameter $b = 0$, 5, and 10 fm, and at times $t = 0$, 0.001 fm/c and 0.01 fm/c. See figures 11 and 12. In figure 11, we see what is expected. At zero impact parameter, there is no preferred direction, so the average net magnetic field is zero, whereas the average magnitude of the magnetic field is not. However, looking at subfigure (c) of 11 and subfigure (c) of 12, the magnetic field in the y-direction seems to behave differently than the field in the x-direction. This may be unexpected, and will be discussed in section 5.

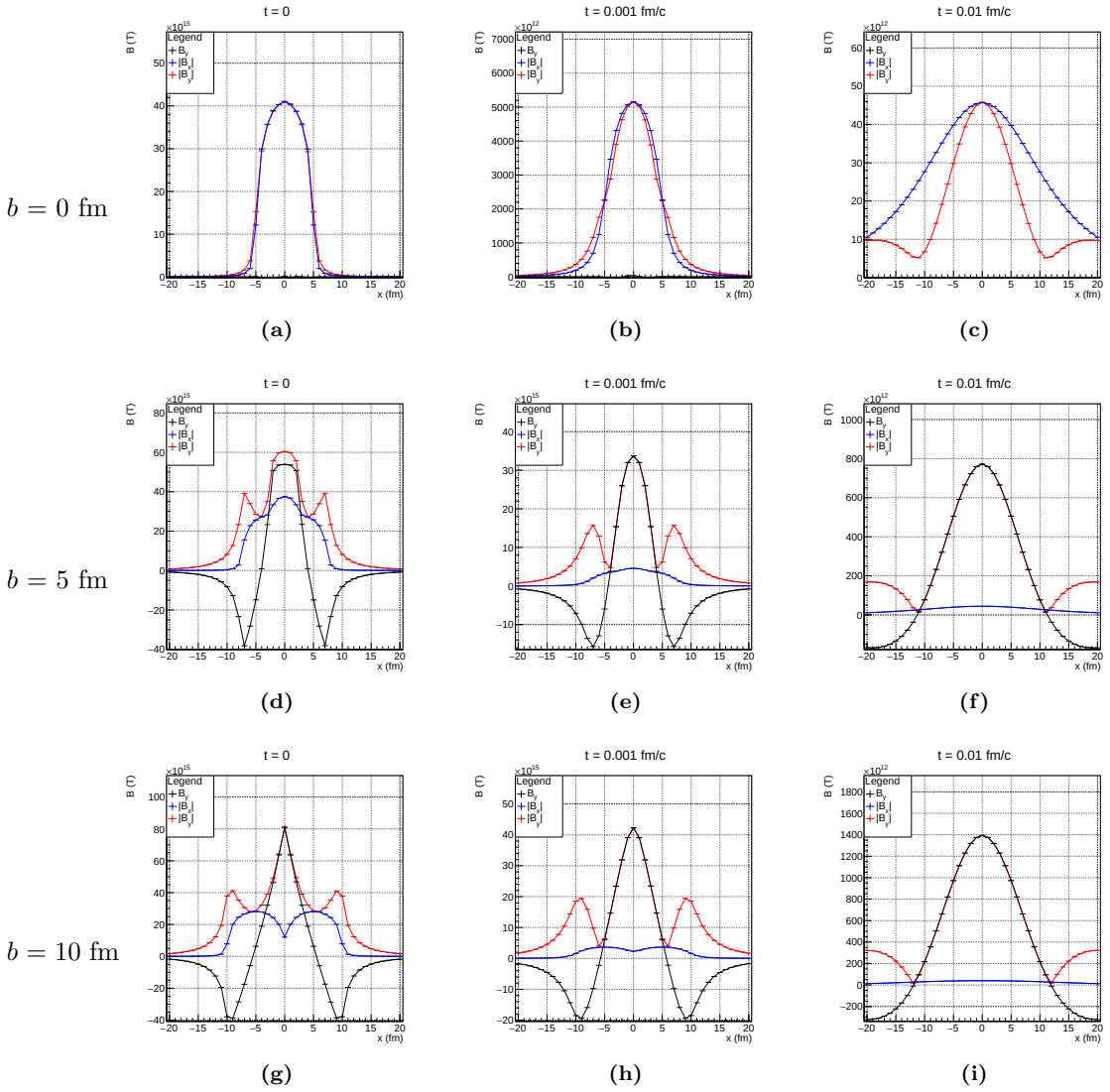

Figure 11: The magnetic field along the x-axis. On the rows from top to bottom, events with impact parameter $b = 0$, 5, and 10 fm are plotted. In the columns, events after 0, 0.001, and 0.01 fm/c are plotted. At later times (e.g. 0.1 or 1 fm/c), the profile flattens out, resulting in horizontal lines (i.e. the spatial dependence goes away).
At zero impact parameter, the average net magnetic field is zero, as there is no spatial dependence. However, in each event, the magnetic field can still be quite large (we see up to 4×10^16 T at collision center). For later times, the magnetic field diminishes quickly.
At nonzero impact parameter, the nuclei are clearly visible as peaks in the average magnitude of B_x. For B_y, we see what is expected: a positive peak at collision center, and a negative peak away from the nuclei. After a short while (0.001 or 0.01 fm/c), the magnetic field diminishes and seems to smooth out.

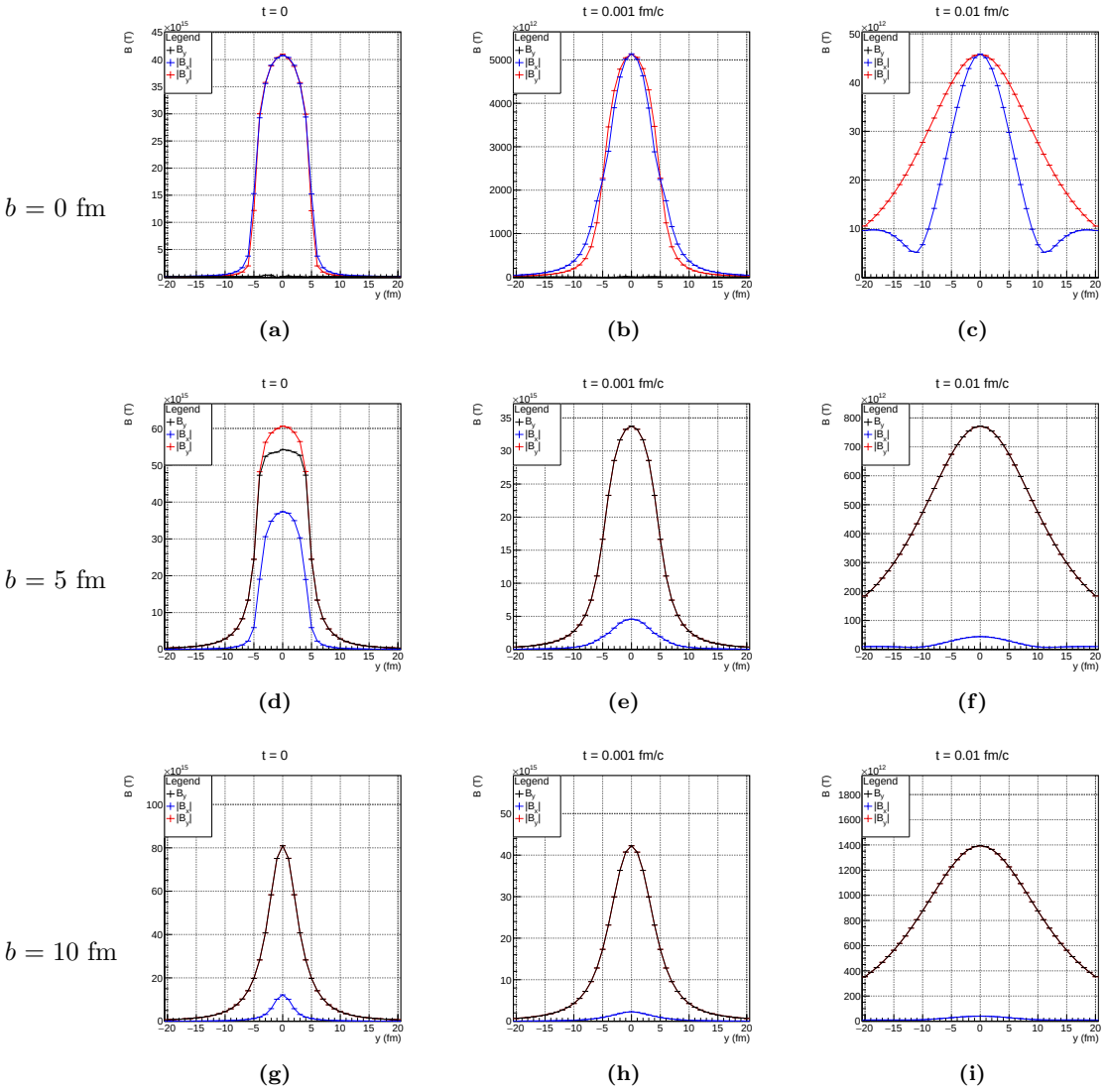

Figure 12: The magnetic field along the y-axis. On the rows from top to bottom, events with impact parameter $b = 0$, 5, and 10 fm are plotted. In the columns, events after 0, 0.001, and 0.01 fm/c are plotted. At later times (e.g. 0.1 or 1 fm/c), the profile flattens out, resulting in horizontal lines (i.e. the spatial dependence goes away).
At zero impact parameter, the average net magnetic field is zero, as there is no spatial dependence. However, in each event, the magnetic field can still be quite large (we see up to 4×10^16 T at collision center). For later times, the magnetic field diminishes quickly.
At nonzero impact parameter, we see a nonzero average net magnetic field, dropping off quickly as we move away from the center.

5 Discussion

While T$_{\text{R}}$ENTo simulates events, the actual way the collision occurs is very crude. In the working model, participants stop at the moment of collision, and the stopped protons' magnetic contribution due to acceleration is ignored. This is done because investigating how relativistic nucleons collide is beyond the scope of this thesis. A slight improvement to the "stopping participants" model is one where participants scatter elastically according to equation A.7 in [6]:

$$f(Y) = \frac{a}{2\sinh(aY_0)} e^{aY}, \qquad -Y_0 \leq Y \leq Y_0.$$

Here $f(Y)$ is the normalized distribution of the rapidities of the participants after collision, where Y_0 is the rapidity of the colliding nuclei, and $a \approx 1/2$. Note that most of the participants have a rapidity of around Y_0, i.e. the rapidity of the spectators. This means that most participants keep moving roughly in the same direction. They can have some radial velocity, which was assumed to be radially away from the origin. Yet, because most participants keep moving in the same direction, the plots of the impact parameter dependence with the "rapidity distribution" are virtually indistinguishable from figure 5, therefore they have not been included.

The main difference between the results obtained with T$_{\text{R}}$ENTo and those from figure 4 is the order of magnitude. While we expect to see a maximum magnetic field of $60m_\pi^2 \approx 6 \times 10^{15}$ T, T$_{\text{R}}$ENTo gives a maximum of 9×10^{16} T. This is more than an order of magnitude and needs an explanation. We do a quick calculation by hand of the magnetic field of a single proton moving at 0.3 fm away from the origin, i.e. $\boldsymbol{r}_c(t') = (0.3 \text{ fm}, 0, vt')$.
First calculate the retarded time at $t = 0$ from equation 2: $c^2(t'-t)^2 = (0.3 \text{ fm}^2 + v^2 t'^2$. This is just a quadratic equation, and solving for t' yields

$$t' = \gamma^2 \left(t - \sqrt{\left(\frac{0.3 \text{ fm}}{\gamma c}\right)^2 + \left(\frac{vt}{c}\right)^2} \right).$$

so at $t = 0$ we have $t' = -0.3 \text{ fm } \gamma/c \approx -441 \text{ fm}/c$.
Now we evaluate the expression for the magnetic field (equation 8) at this time:

$$\begin{aligned} B_y &= \frac{q}{4\pi\varepsilon_0 c} \frac{(\boldsymbol{\beta} \times \boldsymbol{R})_y}{\gamma^2 (R - \boldsymbol{R}\cdot\boldsymbol{\beta})^3} \\ &= 4.8 \times 10^{-18} \text{ T m}^2 \frac{0.3 \text{ fm } \beta}{1470^2 \left(\sqrt{(0.3 \text{ fm})^2 + (v \cdot -441 \text{ fm}/c)^2} - (\beta v \cdot 441 \text{ fm}/c) \right)^3} \\ &\approx 8 \times 10^{16} \text{ T}. \end{aligned}$$

Since most of the magnetic field comes from the closest protons, this serves as a very crude estimate for the expected magnetic field strength in a heavy ion collision (i.e. ignore all other protons in a nucleus). This corresponds to the magnetic fields we observe with T$_{\text{R}}$ENTo. So, the while the results differ from existing literature, T$_{\text{R}}$ENTo is actually working as intended.

Another difference is the different place of the peak of B_y. From figure 4, we expect a maximum B_y at an impact parameter of 12 or 13 fm. With T$_{\text{R}}$ENTo we observe maximum B_y at an impact parameter of about 9 fm. At this point, most of the nucleons from the one nucleus will be on one side, and the nucleons of the other nucleus will be on the other side. At this point we can treat the entire nuclei as two big charges moving past, making the magnetic field drop off quadratically. This is what we see in T$_{\text{R}}$ENTo 's results. While the radius of a lead nucleus is 6.62 fm, this peak should happen before 2 times 6.62 fm, while in figure 4 it seems that the peak is exactly there. The peak should happen before, because the few nucleons at the edge of the nucleus are not relevant with respect to the entire nucleus.

There is also something peculiar about figure 11 (c) and figure 12 (c). At zero impact parameter, we expect a perfectly symmetric head-on collision, so there should be no difference in x- and y-dependence. At collision time $t = 0$ this is indeed the case, however at $t = 0.01$ fm/c, a difference in the x- and y-dependence begins. In the x-direction $|B_y|$ decreases more than $|B_x|$and vice versa. This is because actually, there is a no symmetry between $|B_x|$ and $|B_y|$. That is, there is still a difference between the magnetic field pointing towards/away from a symmetric event and the magnetic field pointing around the symmetric event. Along the x-axis, $|B_y|$ points around the event, whereas along the y-axis, $|B_x|$ points around the event. Indeed, $|B_x|$ and $|B_y|$ switch places in figure 11 (c) and figure 12 (c).

6 Conclusion and Outlook

Magnetic fields in heavy ion collisions can become very big ($\sim 10^{15}$ T [1, 5, 8, 9]). With T$_\text{R}$ENTo these results have been somewhat succesfully replicated, although there are some disagreements with earlier simulations. Most notably with T$_\text{R}$ENTo the magnetic field strength has been found to be an order of magnitude larger. Also, the impact parameter at which the biggest average magnetic field can be expected is slightly less (only 9 fm) than the expected 12 or 13 fm.

The magnetic field along the x- and y-axis have been analyzed (see figure 11 and figure 12 respectively). In the x-direction, at zero impact parameter and at collision time, there is no difference in $|B_x|$ and $|B_y|$ (on average). However, after 0.01 fm/c, there is a clear difference between $|B_x|$ and $|B_y|$, the magnetic field pointing around the nucleus is suppressed, as the two nuclei induce an opposing magnetic field. Furthermore, at zero impact parameter, the average magnetic field outside the nucleus is severely suppressed, and negligible compared to the magnetic field inside the collision (see figures (a)).

Along the x-axis at nonzero impact parameter we see what is expected: a magnetic field pointing in the positive y-direction in the center, and pointing in the negative y-direction just outside the nuclei, and decaying quadratically afterwards.

The magnetic fields are very short-lived, as just 0.01 fm/c away from the collision time, the magnetic field is more than 4 orders of magnitude smaller than before at collision time. See figure 9.

While undoubtedly more can be done with T$_\text{R}$ENTo, we could also set our eyes on other modeling software, such as the UrQMD model, or the Ultrarelativistic Quantum Molecular Dynamics model. This software simulates heavy ion collisions such as those at the RHIC[18]. This model is much more accurate than T$_\text{R}$ENTo because it also takes into account much more advanced properties of matter such as color and quantum effects.

References

[1] VVSK OKOV and VD TONEEV. Estimate of the magnetic field strength in heavy-ion collisions. *arXiv preprint arXiv:0907.1396*, 2009.

[2] J. Scott Moreland, Jonah E. Bernhard, and Steffen A. Bass. Alternative ansatz to wounded nucleon and binary collision scaling in high-energy nuclear collisions. *Phys.Rev.*, C92(1):011901, 2015.

[3] C Loizides, J Nagle, and P Steinberg. Improved version of the phobos glauber monte carlo. *SoftwareX*, 1:13–18, 2015.

[4] ALICE (A Large Ion Collider Experiment). `https://home.cern/about/physics/heavy-ions-and-quark-gluon-plasma`. Accessed: 2017-08-07.

[5] Koichi Hattori and Xu-Guang Huang. Novel quantum phenomena induced by strong magnetic fields in heavy-ion collisions. *arXiv preprint arXiv:1609.00747*, 2016.

[6] DE Kharzeev and LD Mclerran. Effects of topological charge change in heavy ion collisions:'event by event p and cp violation'," nucl. phys. a 803, 227 (2008), arxiv: 0711.0950 [hep-ph]; k. fukushima, de kharzeev and hj warringa. *The Chiral Magnetic Effect Phys. Rev. D*, 78:074033, 2008.

[7] Dmitri E Kharzeev. The chiral magnetic effect and anomaly-induced transport. *Progress in Particle and Nuclear Physics*, 75:133–151, 2014.

[8] Vadim Voronyuk, Viacheslav D Toneev, Wolfgang Cassing, Elena L Bratkovskaya, Volodymyr P Konchakovski, and Sergei A Voloshin. Electromagnetic field evolution in relativistic heavy-ion collisions. *Physical Review C*, 83(5):054911, 2011.

[9] Wei-Tian Deng and Xu-Guang Huang. Event-by-event generation of electromagnetic fields in heavy-ion collisions. *Physical Review C*, 85(4):044907, 2012.

[10] Kenneth Aamodt, A Abrahantes Quintana, R Achenbach, S Acounis, D Adamová, C Adler, M Aggarwal, F Agnese, G Aglieri Rinella, Z Ahammed, et al. The alice experiment at the cern lhc. *Journal of Instrumentation*, 3(08):S08002, 2008.

[11] Kenji Fukushima, Dmitri E Kharzeev, and Harmen J Warringa. Chiral magnetic effect. *Physical Review D*, 78(7):074033, 2008.

[12] John David Jackson. *Classical electrodynamics*. J. Wiley & sons, New York, 1999.

[13] David J Griffiths. Electrodynamics. *Introduction to Electrodynamics, 3rd ed., Prentice Hall, Upper Saddle River, New Jersey*, pages 301–306, 1999.

[14] Ulrich W Heinz and Raimond Snellings. Collective flow and viscosity in relativistic heavy-ion collisions. *arXiv preprint arXiv:1301.2826*, 2013.

[15] T$_{\mathrm{R}}$ENTo: *Reduced Thickness Event-by-event Nuclear Topology*. `http://qcd.phy.duke.edu/trento/internals.html#list-of-classes`. Accessed: 2017-07-16.

[16] Adam Bzdak and Vladimir Skokov. Event-by-event fluctuations of magnetic and electric fields in heavy ion collisions. *Physics Letters B*, 710(1):171–174, 2012.

[17] Michael L Miller, Klaus Reygers, Stephen J Sanders, and Peter Steinberg. Glauber modeling in high-energy nuclear collisions. *Annu. Rev. Nucl. Part. Sci.*, 57:205–243, 2007.

[18] SA Bass, M Belkacem, M Bleicher, M Brandstetter, L Bravina, C Ernst, L Gerland, M Hofmann, S Hofmann, J Konopka, et al. The ultra relativistic quantum molecular dynamics (urqmd) model is a transport model for simu-lating heavy ion collisions in the energy range from sis to rhic. it runs on various unix-based com-puting platforms. current implementations include ibm/aix (xlf), gnu/linux (g77, ifc), sgi/irix, dec-unix and sun/solaris. urqmdis designed

as multipurpose tool for studying a wide variety of heavy ion related effects rang. *J. Phys*, 25:1859–1896, 1999.

[19] Ulrich W Heinz. Concepts of heavy-ion physics. *arXiv preprint hep-ph/0407360*, 2004.

[20] B Alver, M Baker, C Loizides, and P Steinberg. The phobos glauber monte carlo. *arXiv preprint arXiv:0805.4411*, 2008.

[21] David J Griffiths. *Introduction to electrodynamics; 4th ed.* Pearson, Boston, MA, 2013.

[22] T$_{\mathrm{R}}$ENTo: *Reduced Thickness Event-by-event Nuclear Topology.* `https://github.com/Duke-QCD/trento`. Accessed: 2017-01-16.

[23] Aldo Antognini, François Nez, Karsten Schuhmann, Fernando D Amaro, François Biraben, João MR Cardoso, Daniel S Covita, Andreas Dax, Satish Dhawan, Marc Diepold, et al. Proton structure from the measurement of 2s-2p transition frequencies of muonic hydrogen. *Science*, 339(6118):417–420, 2013.

[24] Simon Candelaresi and Axel Brandenburg. Decay of helical and nonhelical magnetic knots. *Physical Review E*, 84(1):016406, 2011.

[25] M Stephanov, K Rajagopal, and E Shuryak. Event-by-event fluctuations in heavy ion collisions and the qcd critical point. *Physical Review D*, 60(11):114028, 1999.

[26] L McLerran and V Skokov. Comments about the electromagnetic field in heavy-ion collisions. *Nuclear Physics A*, 929:184–190, 2014.